An efficient screening strategy towards multifunctional catalysts for the simultaneous electroreduction of NO_3^-, NO_2^- and NO to NH_3

Peng Lv[1,5], Donghai Wu[1], Bingling He[1], Xue Li[1], Rui Zhu[1], Gang Tang[2], Zhansheng Lu[3], Dongwei Ma[1,5*] and Yu Jia[1, 4, 5*]

[1]*Key Laboratory for Special Functional Materials of Ministry of Education, and School of Materials Science and Engineering, Henan University, Kaifeng 475004, China*

[2] *Advanced Research Institute of Multidisciplinary Science, Beijing Institute of Technology, Beijing 100081, China*

[3]*School of Physics, Henan Normal University, Xinxiang 453007, China*

[4]*International Laboratory for Quantum Functional Materials of Henan, and School of Physics, Zhengzhou University, Zhengzhou 450001, China*

[5]*Laboratory for Quantum Materials of Henan, and Center for Topological Functional Materials, Henan University, Kaifeng 475004, China*

---

* Corresponding author. E-mail: madw@henu.edu.cn

* Corresponding author. E-mail: jiayu@henu.edu.cn

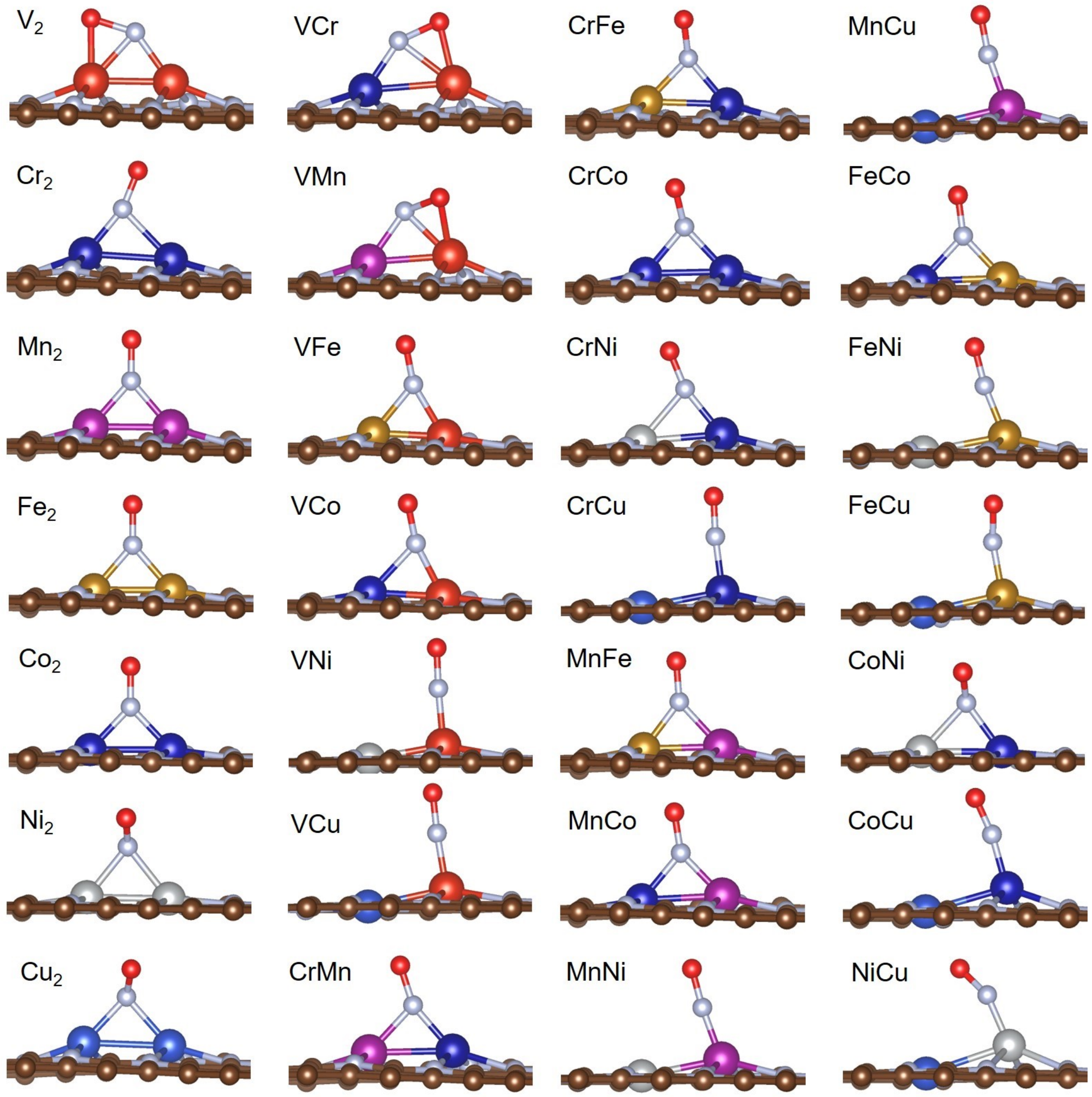

Fig. S1. The most stable *NO configurations over M1M2@NG DACs.

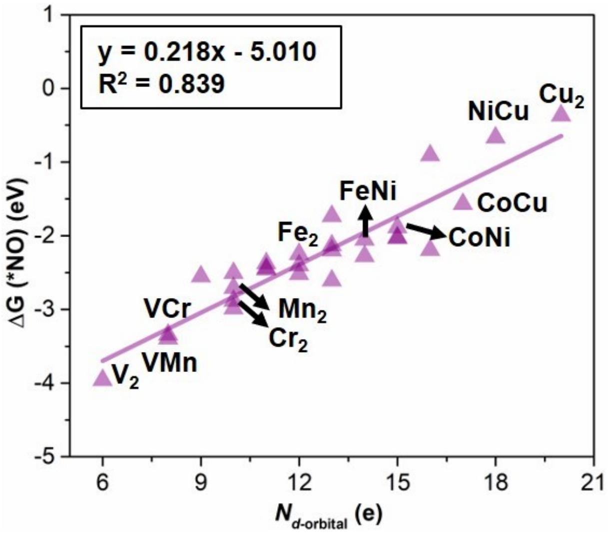

Fig. S2. The relationship between the total number of *d*-orbital valence electrons ($N_{d\text{-orbital}}$, e) of free metal-dimer atoms and free energy change (ΔG (*NO), eV) of the most favorable *NO configurations on each M1M2@NG. These values come from all the 28 M1M2@NG DAC candidates (M1/M2 = V, Cr, Mn, Fe, Co, Ni, and Cu).

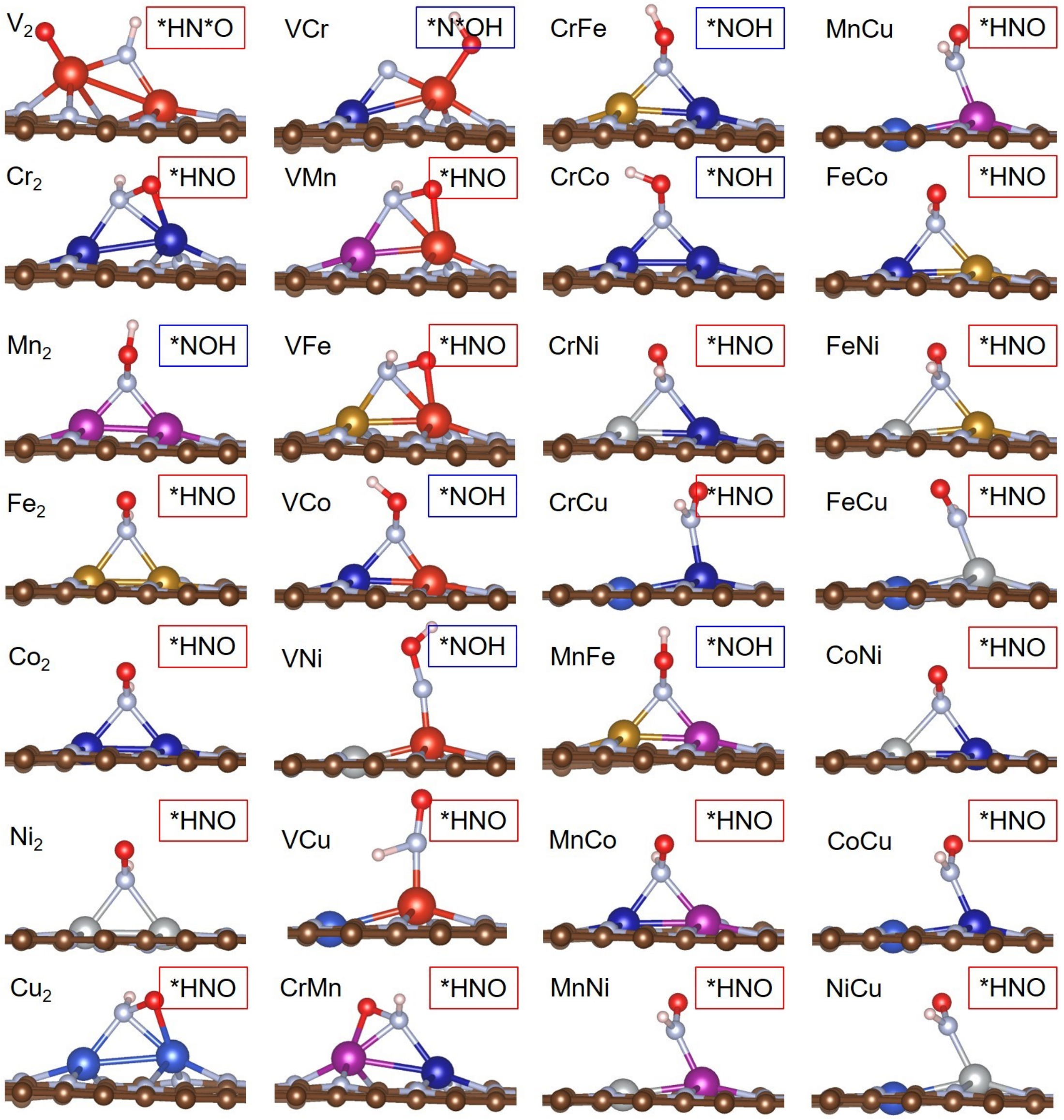

Fig. S3. The most stable *HNO/*NOH configurations over M1M2@NG DACs.

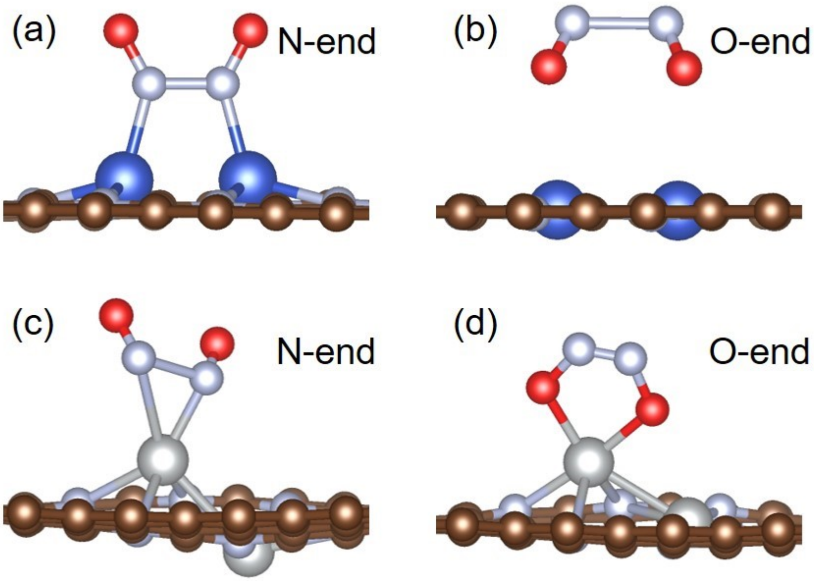

Fig. S4. The structures of $*N_2O_2$ with N-end and O-end configurations over (a-b) Cu_2 and (c-d) Ag_2 DACs.

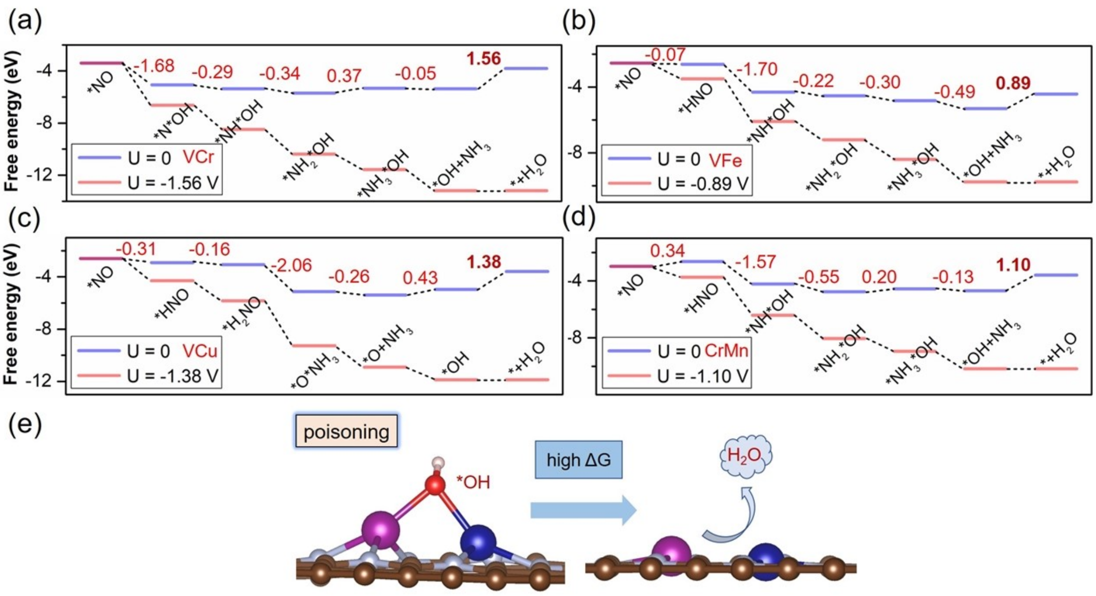

Fig. S5. The free energy diagrams for the NORR towards NH_3 over (a) VCr, (b) VFe, (c) VCu, and (d) CrMn DACs, respectively. The corresponding free energy changes of the key steps along the reaction pathways are presented and the ΔG_{max} values of PDS are in bold. (e) The schematic diagram of poisoning of active sites due to high ΔG of $*OH \rightarrow * + H_2O$.

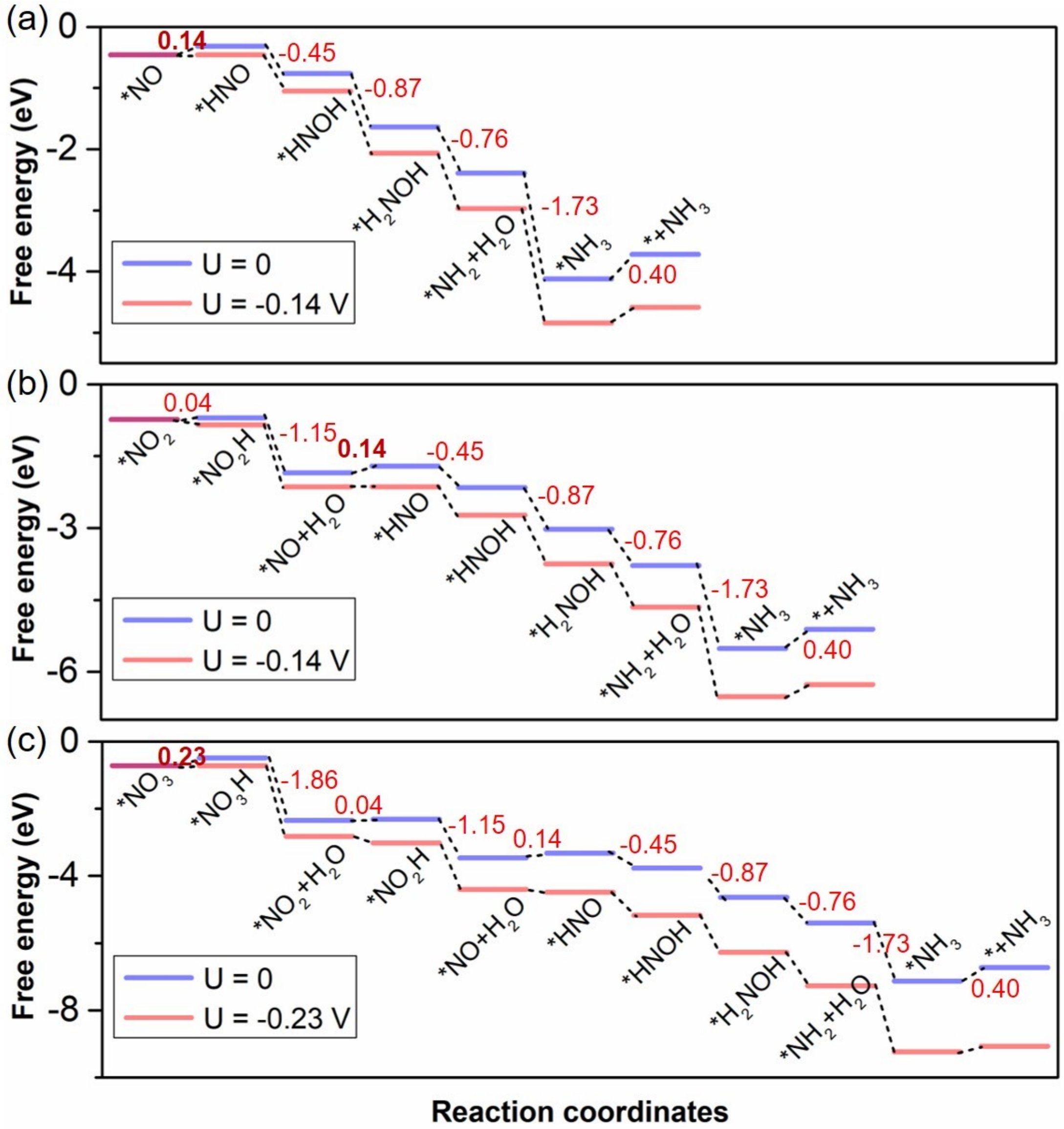

Fig. S6. The free energy diagrams for the (a) NORR, (b) NO_2RR, and (c) NO_3RR towards NH_3 over Ag_2 DAC *via* the most relevant mechanisms. The corresponding free energy changes of the key steps along the reaction pathway are presented and the ΔG_{max} values of potential-determining step are in bold.

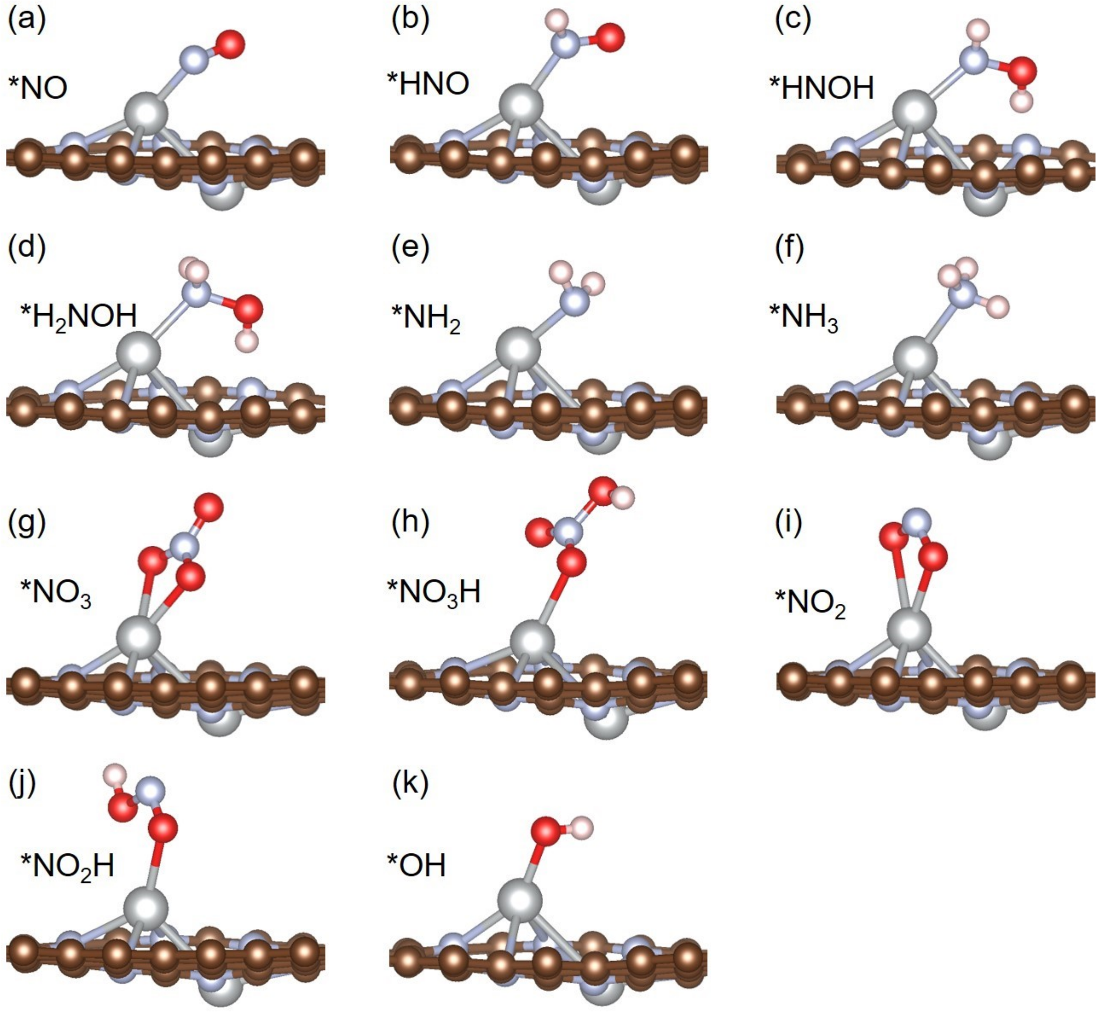

Fig. S7. The most stable configurations for (a) *NO, (b) *HNO, (c) *HNOH, (d) $*H_2NOH$, (e) $*NH_2$, (f) NH_3, (g) $*NO_3$, (h) $*NO_3H$, (i) $*NO_2$, (j) $*NO_2H$, and (k) *OH over Ag_2 DAC.

Table S1. The work flows for the proposed screening strategy according to the step of “stability of catalyst” (I); “NO adsorption” (II) with $\Delta G(*NO) < 0$ and $\Delta G(*NO) < \Delta G(*H)$; “NORR activity” (III) with $\Delta G(*NO \rightarrow *HNO/*NOH) < 0.4$ eV (III-A), $\Delta G(*NH_2 \rightarrow *NH_3)$ and $\Delta G(*OH \rightarrow H_2O) < 0.4$ eV (III-B); “NH_3 selectivity” (IV) with $2\Delta G(*NO) < \Delta G(*N_2O_2)$. When one step does not meet the criteria, the exploration of this DAC system will be interrupted. For Rh_2, Pd_2, Ir_2 and Pt_2 DAC candidates, the “stop” steps are in “NORR activity” (III-A) while in “NO adsorption” (II) for Au_2 DAC.

Screening step	Energy (eV)	Rh_2	Pd_2	Ag_2	Ir_2	Pt_2	Au_2
I	E_b	-13.02	-9.16	-5.20	-15.09	-12.90	-5.82
II	$\Delta G(*NO)$	-1.96	-0.68	-0.46	-1.89	-0.86	**0.58 (stop)**
	$\Delta G(*H)$	-0.06	-0.07	0.86	-0.14	-0.49	
III-A	$\Delta G(*NO \rightarrow *HNO/*NOH)$	**0.91 (stop)**	**0.81 (stop)**	0.14	**0.82 (stop)**	**0.64 (stop)**	
III-B	$\Delta G(*NH_2 \rightarrow *NH_3)$			-1.73			-
	$\Delta G(*OH \rightarrow H_2O)$	-	-	-1.41	-	-	-
IV	$2\Delta G(*NO)$	-	-	-0.92	-	-	-
	$\Delta G(*N_2O_2)$	-	-	-0.45	-	-	-
Multifunctional catalytic ability	$\Delta G(*NO_3 \rightarrow *NO_3H)$	-	-	0.23	-	-	-
	$\Delta G(*NO_2 \rightarrow *NO_2H)$	-	-	0.04	-	-	-

Note S2. The solvation effect for the electrocatalytic activity

The structure of two explicit water molecules near the active site in the hybrid model are shown in the **Fig. S8**. Then we used the continuum solvation model[1] to investigate the solvation effect on the NO_xRR. Like this, the combination of explicit water molecules and continuum solvation model are called as hybrid method for solvation effect[2,3]. The solvation energies for different adsorbed species are shown in the **Table S2**. These values from hybrid model are all negative, indicating that the solvent can stabilize the adsorbates in solution. The free energy diagrams for the NORR, NO_2RR, and NO_3RR towards NH_3 over Cu_2 and Ag_2 DAC are shown in **Fig. S9** and **Fig. S10**. The solvation effect does not alter their potential-determining step and the limiting potentials for NORR, NO_2RR, and NO_3RR are still low (-0.19, -0.10, and -0.37 V over Cu_2 DAC; -0.03, -0.03, and -0.24 V over Ag_2 DAC). Moreover, the solvation effect has a small influence on the key protonation steps when using the strategy to screen the multifunctionally electrocatalytic ability for NO_3RR, NO_2RR, and NORR, because the free energy of the two states before and after the key step changes synchronously.

Table S2. Solvation energies (ΔE_{sol}, eV) for different adsorbed species. $\Delta E_{sol} = E_{sol} - E_{vacuum}$, where E_{sol} and E_{vacuum} denote the adsorption energies of adsorbed species with solvation and vacuum, respectively.

Species	ΔE_{sol} from hybrid model	ΔE_{sol} from explicit model in Ref	E_{sol} from implicit model
*NO	-0.04	-0.03 [4]	0.11
*OH	-0.18	-0.41 [5] -0.27~-0.14 [6]	-0.03
*HNO	-0.15	-0.23 [5]	-0.07
*NOH	-0.17	-0.31 [5]	-0.07
*H_2NO	-0.11	-0.24 [5]	0.16
*HNOH	-0.16	-0.47 [5]	-0.22
*H_2NOH	-0.22	-0.41 [7]	-0.38
*NH_2	-0.06	-0.24 [5]	-0.16
*NH_3	-0.14	-0.16 [5]	0.46
*NO_3	-0.27	-	-0.37
*NO_3H	-0.26	-	0.12
*NO_2	-0.22	-	-0.35
*NO_2H	-0.44	-	-0.08

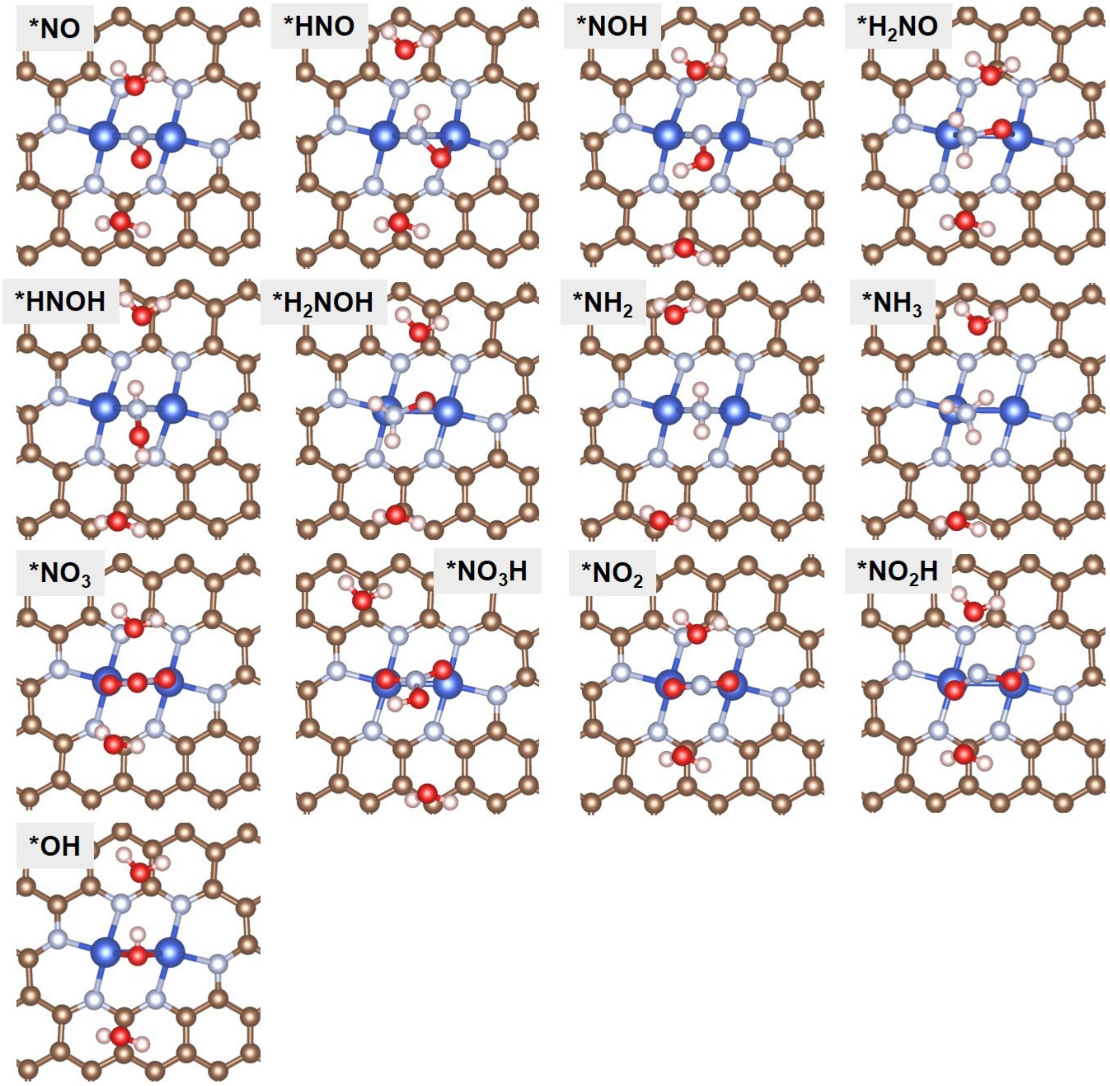

Fig. S8. The explicit structure model with two explicit water molecules near the active site for various adsorbed species.

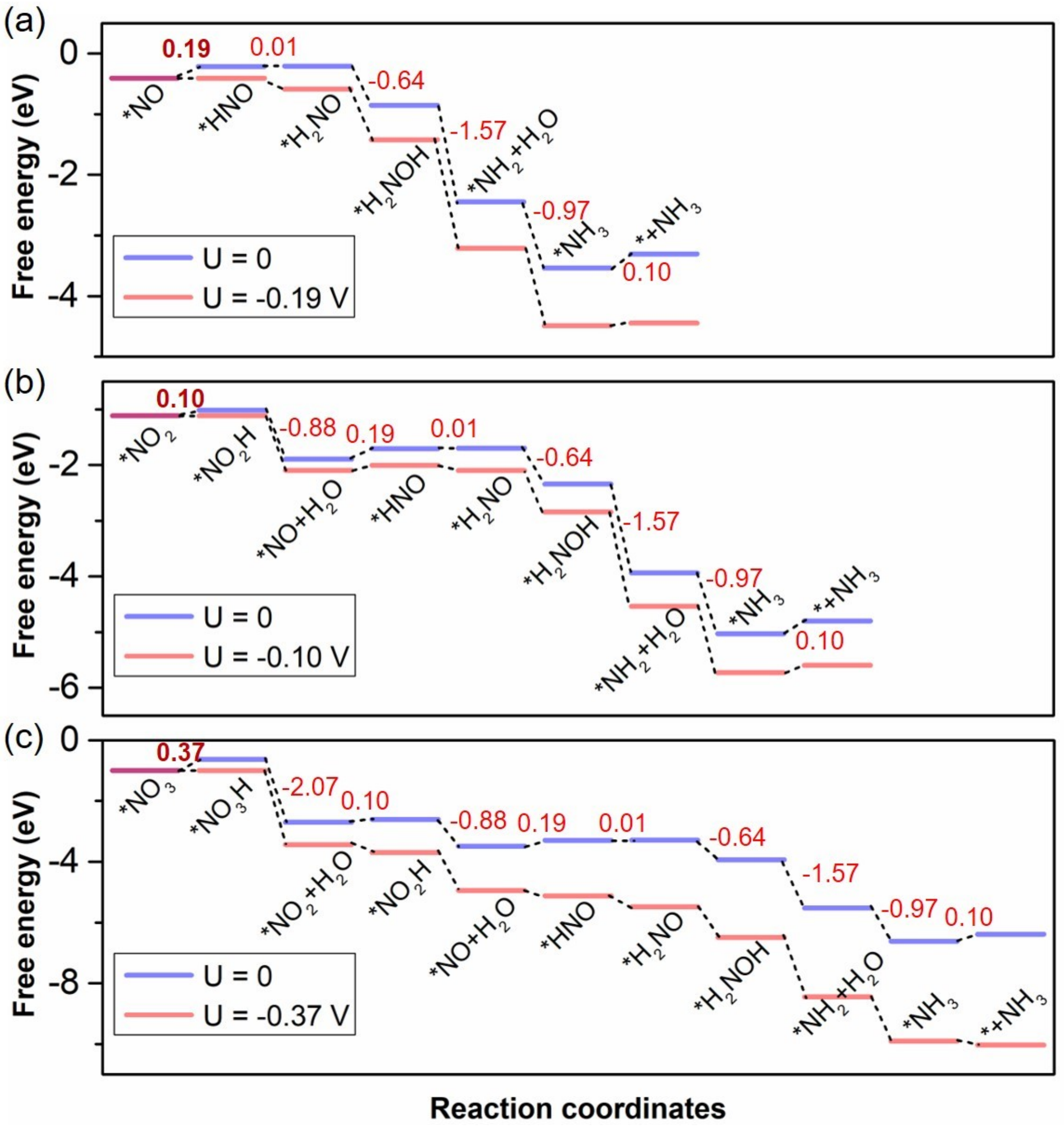

Fig. S9. The free energy diagrams with solvation effect for the (a) NORR, (b) NO_2RR, and (c) NO_3RR towards NH_3 over Cu_2 DAC *via* the most relevant mechanisms. The corresponding free energy changes of the key steps along the reaction pathway are presented and the ΔG_{max} values of potential-determining step are in bold.

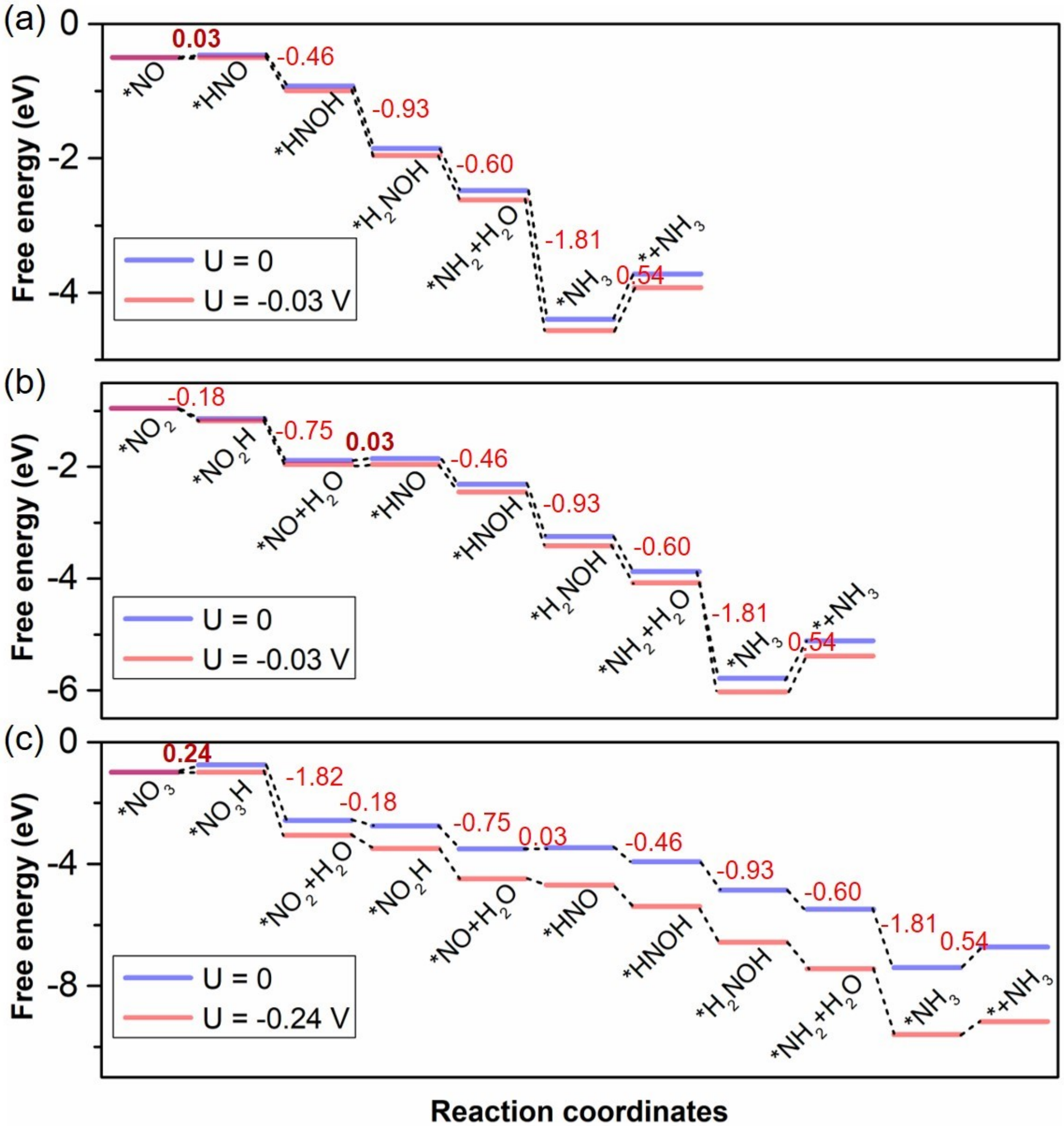

Fig. S10. The free energy diagrams with solvation effect for the (a) NORR, (b) NO_2RR, and (c) NO_3RR towards NH_3 over Ag_2 DAC *via* the most relevant mechanisms. The corresponding free energy changes of the key steps along the reaction pathway are presented and the ΔG_{max} values of potential-determining step are in bold.

Note S2. The pH effect for the electroactivity

For the thermodynamics of electrocatalytic reaction, pH effect can correct the free energy of H^+ by the concentration. Its contribution for the free energy can be determined as $\Delta G_{pH} = \ln 10 \times k_BT \times pH$ (Here k_B is the Boltzmann constant. At room temperature, $\Delta G_{pH} = 0.06 \times pH$) [8]. Thus, as the free energies along each step can be shifted up or down, the limiting potential (U_L) will be changed by the pH effect: $U_L = -(\Delta G_{max}\ (pH=0) + 0.06 \times pH)$. However, according to the Nernst equation, the equilibrium potential (U_e) of NO_xRR can also be changed by the pH effect: $U_e = U_e\ (pH=0) - 0.06 \times pH$. Thus, the overpotential (η) of NO_xRR will be not changed by pH effect, because $\eta = U_e - U_L = [U_e\ (pH=0) - 0.06 \times pH] - [-(\Delta G_{max}\ (pH=0) + 0.06 \times pH)] = U_e\ (pH=0) + \Delta G_{max}\ (pH=0)$. Also, the same trend applies to competitive reaction of HER, indicating that pH effect does not also affect the selectivity[9]. Therefore, NO_xRR can thermodynamically occurs over Cu_2 DAC. Similar phenomena can be found for N_2 reduction over Mo doped graphene[10].

For the NO_xRR in an acidic (alkaline) electrolyte, H_3O^+ (H_2O) acts as the proton donor. Thus, we also considered the dynamic feasibility for the potential-determining step by *NO (*HNO) surrounded by a long-distance H_3O^+ (OH^-). As shown in **Fig. S11a-b**, the initial configuration *NO with H_3O^+ and *HNO with OH^- will be automatically relaxed to the *HNO with H_2O and *NO with H_2O, indicating the easy protonation for the *NO from H_3O^+ under the acidic medium and easy capture of H^+ from the *HNO to free OH^- (difficult protonation for *NO from H_2O) under the alkaline medium. We also tested the dissociation of H_2O under the active site and it shows that the energy barrier is rather high with 2.43 eV (**Fig. S11c**), meaning that adsorbed species for NO_xRR and HER can't obtain the protons from the water molecule under the alkaline medium. These results suggested the dynamic feasibility (infeasibility) for NO_xRR under the acidic (alkaline) medium. Thus, the Cu_2 and Ag_2 DACs are the excellently acidic electrocatalysts to multifunctionally reduce all the NO_x species.

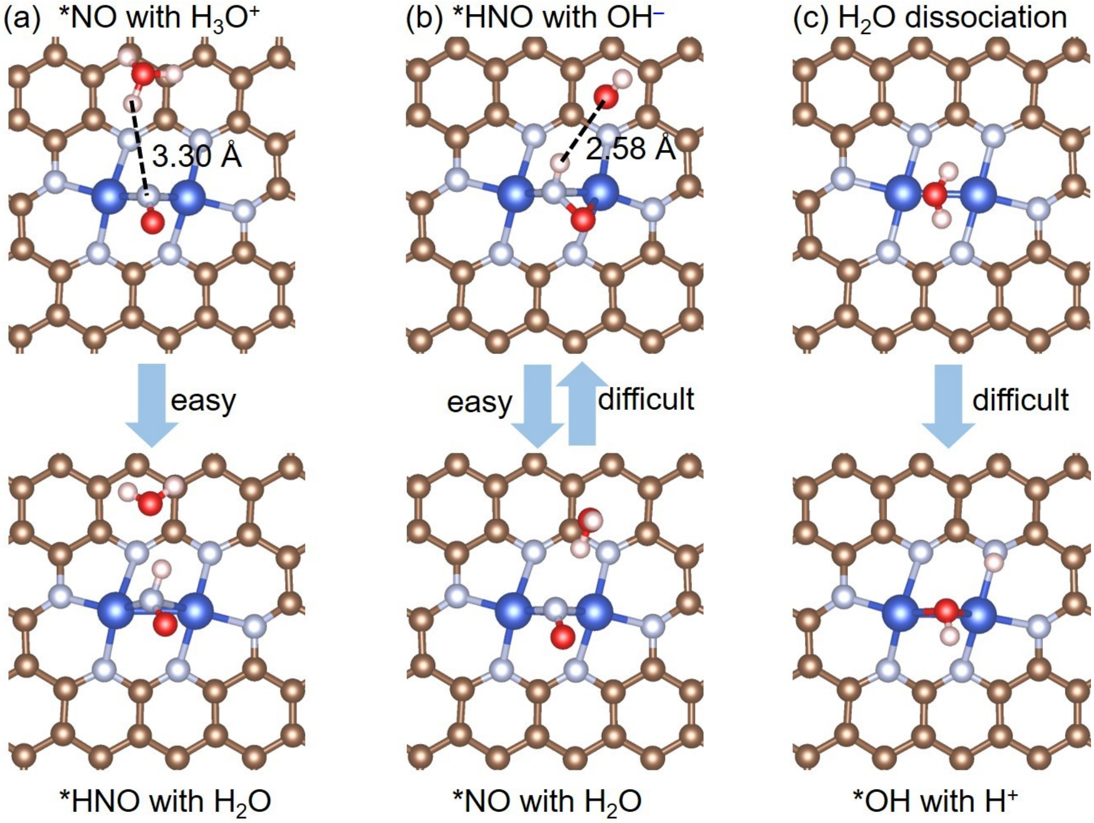

Fig. S11. (a) Easy protonation for *NO from H_3O^+ under the acidic medium. (b) Easy capture of H^+ from the *HNO to free OH^- (difficult protonation for *NO from H_2O) under the alkaline medium. (c) Difficult dissociation of H_2O to form *OH with H^+ under the alkaline medium.

Note S3. The results by used the AIMD method.

Through our screening strategy, Cu_2 and Ag_2@NG were found to have the high electrocatalytic activity for NO_xRR. Thus, we have examined the structural stability of Cu_2 and Ag_2 DACs at 500, 700, and 1000 K by the ab initio molecular dynamics simulations (AIMD) for 10 ps with the current used supercell (7 × 7) of graphene. As shown in **Fig S12** and **Fig S13**, it is found that the energy only shows the periodical fluctuation during the entire period of simulation. Simulation snapshots of the Cu_2 and Ag_2 DACs monolayers at 500, 700, and 1000 K also show their structural integrity up to 10 ps, implying their thermal stability.

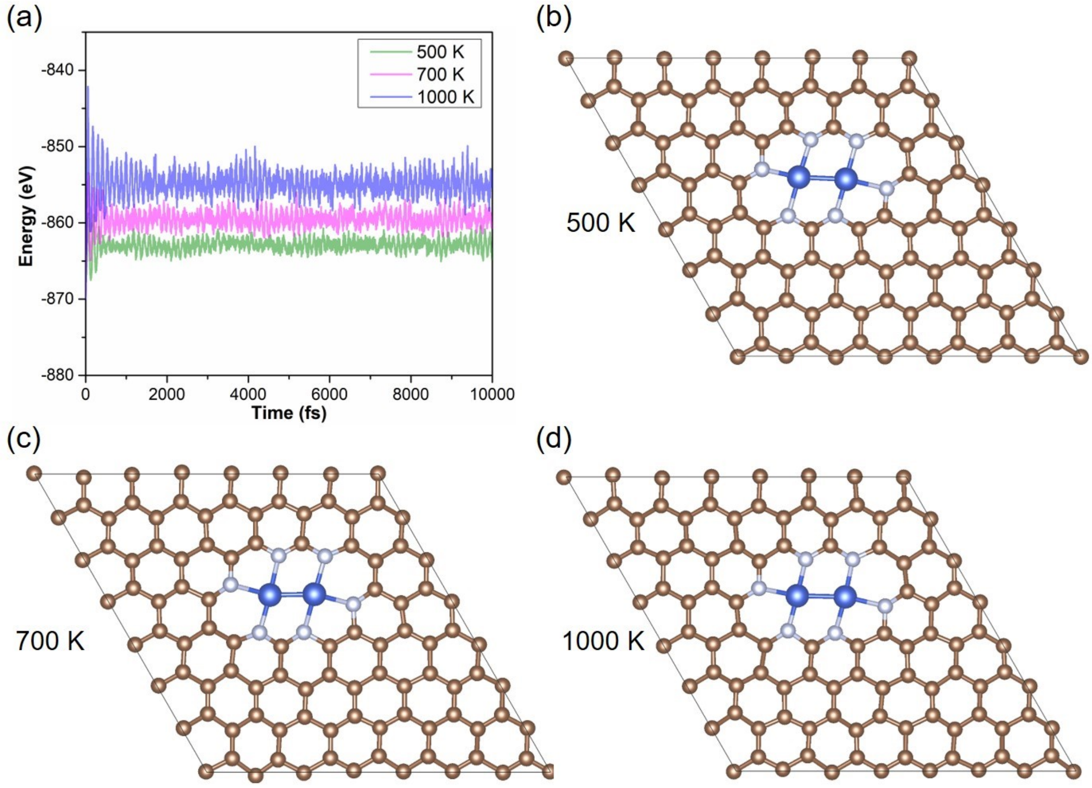

Fig S12. (a) The total energy (eV) fluctuations of the Cu_2@NG with the 7 × 7 supercells of graphene during the AIMD simulations at 500, 700, 1000 K. The simulation was performed for 10 ps with a time-step of 2 fs. The top views of the final configuration after the simulation are shown in (b) 500, (c) 700, (d) 1000 K, respectively.

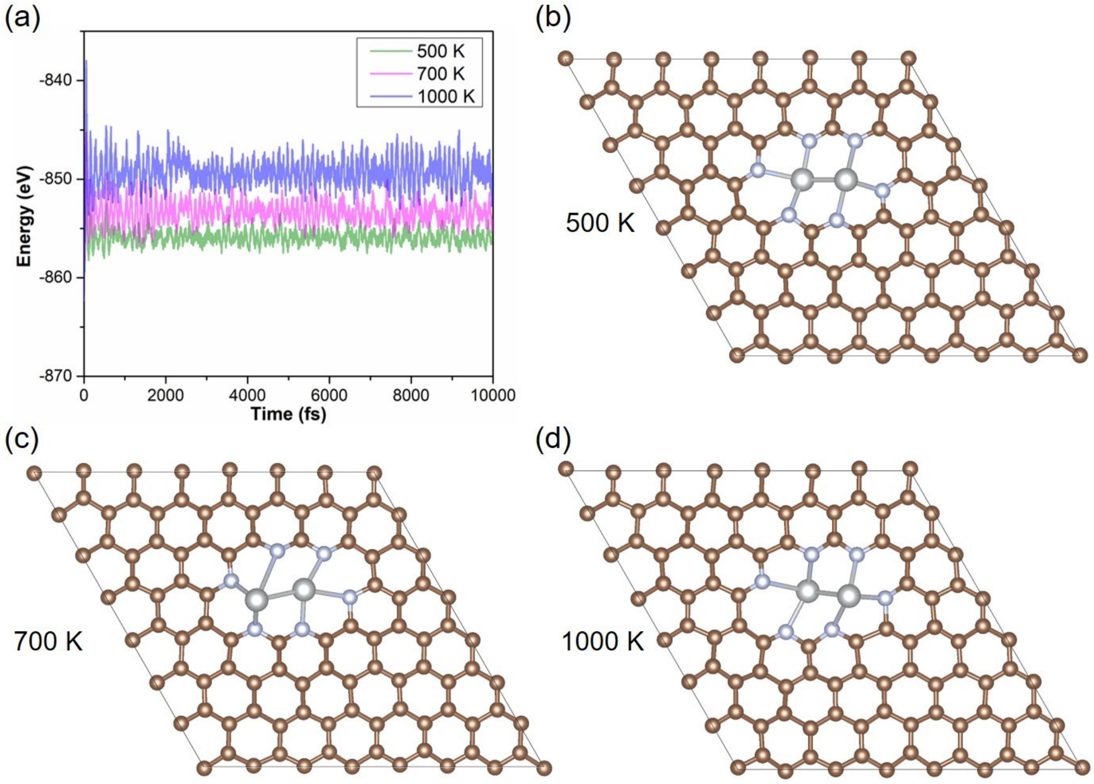

Fig S13. (a) The total energy (eV) fluctuations of the Ag_2@NG with the 7 × 7 supercells of graphene during the AIMD simulations at 500, 700, 1000 K. The simulation was performed for 10 ps with a time-step of 2 fs. The top views of the final configuration after the simulation are shown in (b) 500, (c) 700, (d) 1000 K, respectively.

Note S4. The descriptor analysis for chemical and electrocatalytic activity

Spin and charge states can be helpful for understanding the catalytic mechanism and building a simple descriptor[11], which allows for the design of new catalysts more efficiently. We noted that the charge[12] and spin states[13] of metal atoms can indeed tune the electronic structure and then affect the adsorption strength of reactants, which determine the catalytic performance of catalysts. Here from **Fig. S14a-b**, we found that the DAC systems that have less charge transfers (lower valence state of metal atoms) between metal atoms and N-doped graphene and less magnetic moment of supported metal dimers without molecular adsorption give rise to the lower ΔG_{max} (higher electrocatalytic activity). This arises from the fact that less charge transfer and magnetic moment induce the lower chemical activity, which may give the relatively weaker chemisorption for NO (**Fig. S14c-d**) and higher electrocatalytic activity. However, the former has the better linear scaling relationship with the R^2 of 0.618 (**Fig. S14a**) and 0.700 (**Fig. S14c**).

The partially filled *d*-orbitals are essential for spin magnetism of transition-metal ions[14,15], indicating the spin magnetic moment of transition-metals in the same row are closely related to the atomic numbers. For example, V, Cr, Mn and Fe atoms in the ferromagnetic compounds usually have the possibility for large magnetic moment[16,17]. And the charger transfers between metal and support (or valence state of metal atoms) are affected by the number of electrons in the outermost *d*-shells[18]. Thus, both the spin and charge states reflect to the natural feature of metal atom, *i.e.*, the total number of *d*-orbital electrons (**Fig. S14e-f**). Finally, we showed a reasonable linear relationship with $R^2 = 0.839$ between the obtained NO adsorption strength and ΔG_{max} values (**Fig. S14g**) for NORR towards NH_3 over various DACs. Based on the spin and charge analysis of scaling relationship, we provided a simple and approximate descriptor to evaluate the electrocatalytic activity of current DAC systems for NORR, which don't need to do the DFT calculations to get.

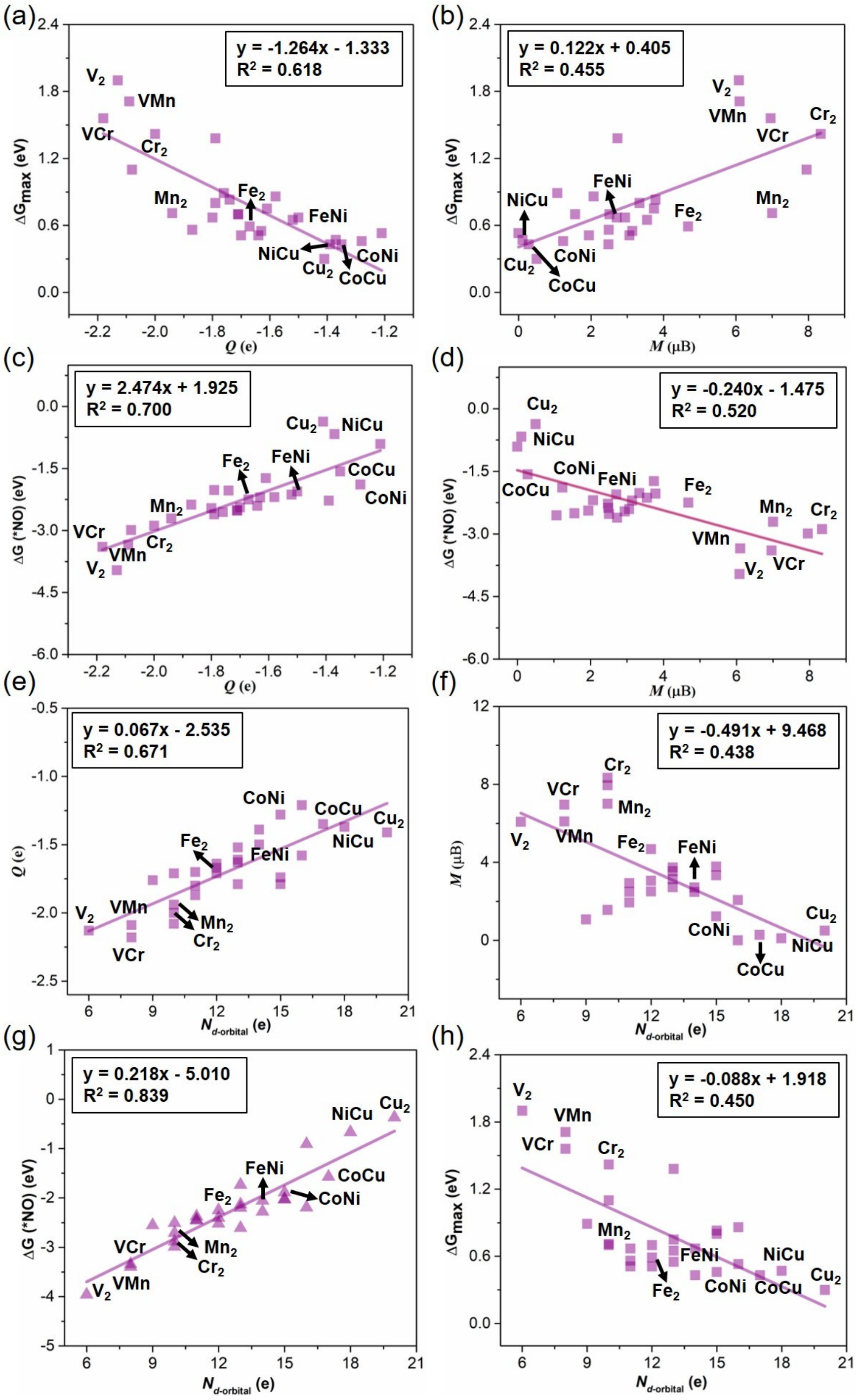

Fig. S14. The relationship between the (a) electrocatalytic activity (ΔG_{max}) of NORR and charge transfer (Q, e), and (b) magnetic moment (M, μB). (c) The relationship between the free energy change of NO adsorption (ΔG (*NO), eV) and Q, and (d) M. (e) The relationship between the Q and total number of d-orbital valence electrons ($N_{d\text{-orbital}}$) of free metal-dimer atoms. (f) The relationship between the M and $N_{d\text{-orbital}}$. (g) The relationship between the ΔG (*NO) and $N_{d\text{-orbital}}$, reproduced by **Fig. S2**. (h) The relationship between the ΔG_{max} and $N_{d\text{-orbital}}$, reproduced by **Fig. 5c**. These values come from all the 28 M1M2@NG DAC candidates (M1/M2 = V, Cr, Mn, Fe, Co, Ni, and Cu).

References

1 K. Mathew, R. Sundararaman, K. Letchworth-Weaver, T. A. Arias and R. G. Hennig, *J. Chem. Phys.*, 2014, **140**, 084106.

2 G. Brancato, N. Rega and V. Barone, *J. Chem. Phys.*, 2008, **128**, 144501.

3 Y. Wang, X. Qin and M. Shao, *J. Catal.*, 2021, **400**, 62–70.

4 J. Long, C. Guo, X. Fu, H. Jing, G. Qin, H. Li and J. Xiao, *J. Phys. Chem. Lett.*, 2021, **12**, 6988–6995.

5 A. Clayborne, H. Chun, R. B. Rankin and J. Greeley, *Angew. Chem.*, 2015, **127**, 8373–8376.

6 M. Reda, H. A. Hansen and T. Vegge, *Catal. Today*, 2018, **312**, 118–125.

7 S. Deshpande and J. Greeley, *ACS Catal.*, 2020, **10**, 9320–9327.

8 W. Zhang, K. Mao and X. C. Zeng, *ACS Sustain. Chem. Eng.*, 2019, **7**, 18711–18717.

9 A. S. Malik, T. Liu, M. Dupuis, R. Li and C. Li, *J. Phys. Chem. C*, 2020, **124**, 8094–8100.

10 J. Zhao and Z. Chen, *J. Am. Chem. Soc.*, 2017, **139**, 12480–12487.

11 A. Kulkarni, S. Siahrostami, A. Patel and J. K. Nørskov, *Chem. Rev.*, 2018, **118**, 2302–2312.

12 Y. Shi, Z.-R. Ma, Y.-Y. Xiao, Y.-C. Yin, W.-M. Huang, Z.-C. Huang, Y.-Z. Zheng, F.-Y. Mu, R. Huang, G.-Y. Shi, Y.-Y. Sun, X.-H. Xia and W. Chen, *Nat. Commun.*, 2021, **12**, 3021.

13 H. Sun, M. Wang, X. Du, Y. Jiao, S. Liu, T. Qian, Y. Yan, C. Liu, M. Liao, Q. Zhang, L. Meng, L. Gu, J. Xiong and C. Yan, *J. Mater. Chem. A*, 2019, **7**, 20952–20957.

14 F. Ye, J. Wang, J. Sheng, C. Hoffmann, T. Gu, H. J. Xiang, W. Tian, J. J. Molaison, A. M. dos Santos, M. Matsuda, B. C. Chakoumakos, J. A. Fernandez-Baca, X. Tong, B. Gao, J. W. Kim and S.-W. Cheong, *Phys. Rev. B*, 2018, **97**, 041112.

15 J.-J. Zhang, L. Lin, Y. Zhang, M. Wu, B. I. Yakobson and S. Dong, *J. Am. Chem. Soc.*, 2018, **140**, 9768–9773.

16 B. Huang, G. Clark, E. Navarro-Moratalla, D. R. Klein, R. Cheng, K. L. Seyler, D. Zhong, E. Schmidgall, M. A. McGuire, D. H. Cobden, W. Yao, D. Xiao, P. Jarillo-Herrero and X. Xu, *Nature*, 2017, **546**, 270–273.

17 V. V. Kulish and W. Huang, *J. Mater. Chem. C*, 2017, **5**, 8734–8741.

18 D. Ma, Y. Wang, L. Liu and Y. Jia, *Phys. Chem. Chem. Phys.*, 2021, **23**, 4018–4029.